

# Multiobjective Optimization of Silver-Nanowire Deposition for Flexible Transparent Conducting Electrodes

Mark Lee, Robert T. Piper, Bishal Bhandari, and Julia W. P. Hsu\*

Cite This: *ACS Appl. Nano Mater.* 2023, 6, 17364–17368

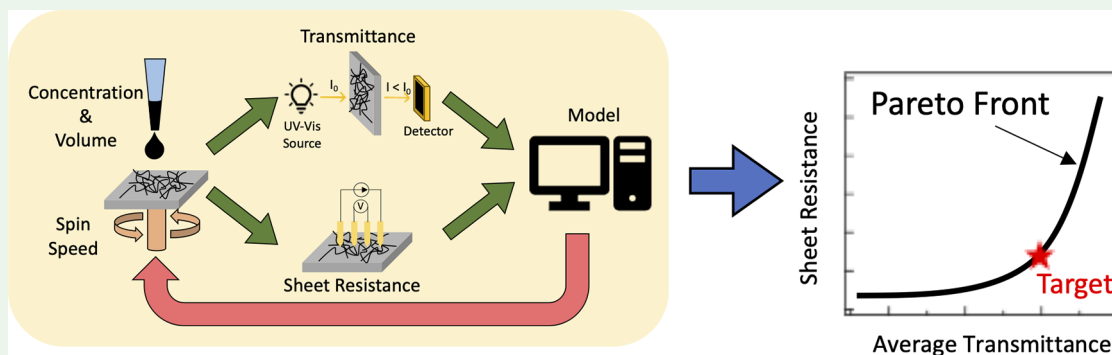
Read Online

ACCESS |

Metrics &amp; More

Article Recommendations

Supporting Information



**ABSTRACT:** Optimizing the spin coating of silver nanowires to form transparent conducting electrodes (TCE) is guided by machine learning (ML). A good TCE has two competing characteristics: high transmittance and high conductance. Optimization using a scalar figure of merit, as often done in the field, cannot satisfy the independent requirements for transmittance and conductance imposed by specific applications. By performing a Pareto front analysis based on ML models, we show that the desired outcomes of transmittance  $\geq 75\%$  and sheet resistance  $\leq 15 \Omega/\text{sq}$  are challenging but can be achieved using processing parameters identified by ML analysis.

**KEYWORDS:** Transparent conducting electrodes, Silver nanowires, Machine learning, Gaussian process, Multiobjective optimization, Pareto front, Figure of merit

Transparent conducting electrodes (TCEs) play a crucial role in applications such as light-emitting diodes (LEDs), photovoltaics (PVs), and touch screens.<sup>1,2</sup> Additionally, flexible TCEs made on plastic substrates such as poly(ethylene terephthalate) (PET) are desired for the Internet of Things, flexible electronics, and curved displays. Three common types of flexible TCEs are transparent conducting oxide films such as indium tin oxide (ITO), metal grids, and metal nanowires.<sup>2</sup> A good TCE should have a high transmittance and high conductance simultaneously. Because high electrical conductivity implies strong optical reflectance and absorption, achieving simultaneously high conductivity and high transparency poses a major challenge in TCE development. For example, a higher filling factor in metal grids increases the conductance but lowers transmittance. Similarly, increasing the ITO film thickness improves conductance but reduces transmittance. In our effort, a layer of silver nanowires (AgNWs) is combined with transparent indium zinc oxide (IZO) sol–gel films to enhance IZO film conductance,<sup>3</sup> with the goal of meeting minimum sheet conductance requirements for TCEs used in LEDs and PVs.

In TCE research, a scalar figure of merit (FOM) that combines transmittance ( $T$ ) and sheet conductance ( $G_{\text{sq}}$ ) or

resistance ( $R_{\text{sq}} = 1/G_{\text{sq}}$ ) is commonly used to quantify their performance.<sup>4,5</sup> The relative importance of  $T$  and  $G_{\text{sq}}$  depends on how the FOM is defined. For example, the ratio between DC and optical conductivities forms a unitless FOM:<sup>6</sup>

$$\text{FOM}_{\text{unitless}} = \frac{\sigma_{\text{DC}}}{\sigma_{\text{opt}}} = (188.5 \Omega) \frac{G_{\text{sq}}}{T^{-1/2} - 1} = \frac{188.5 \Omega}{R_{\text{sq}}(T^{-1/2} - 1)} \quad (1)$$

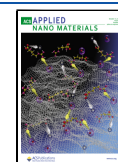
where  $188.5 \Omega$  is half of the vacuum impedance.  $\text{FOM}_{\text{unitless}}$  gives greater weight to a higher  $G_{\text{sq}}$ . Another commonly used FOM<sup>7</sup> emphasizes transmittance by using  $T^{10}$ :

$$\text{FOM}_{T^{10}} = T^{10} G_{\text{sq}} = \frac{T^{10}}{R_{\text{sq}}} \quad (2)$$

Received: August 2, 2023

Accepted: September 19, 2023

Published: October 2, 2023



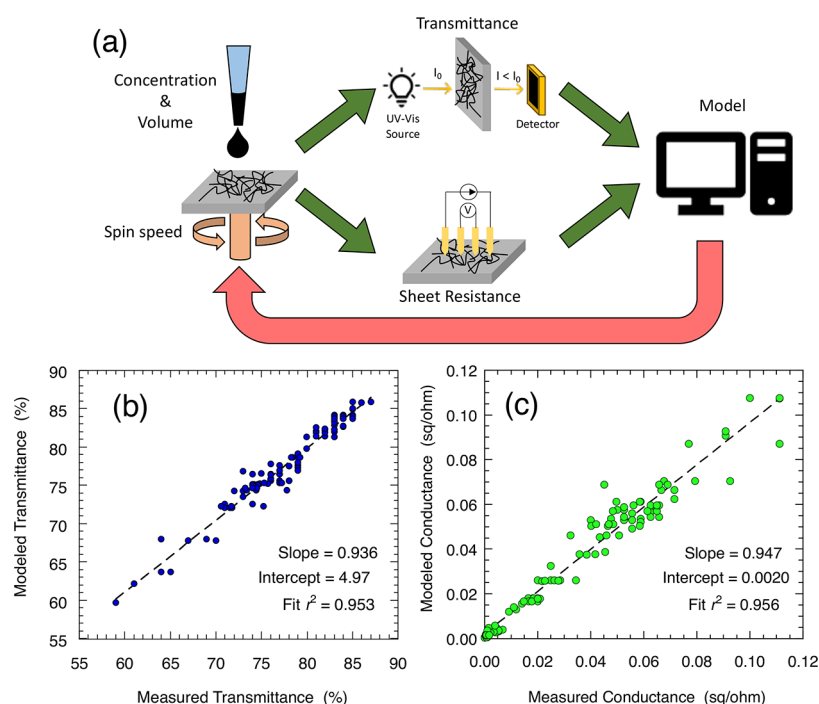


**Figure 1.** (a) Schematic workflow of the experiment. Parity plot for the GPR model of (b) transmittance and (c) sheet conductance.

Comparing TCE performance among works using different FOMs is difficult.<sup>4,5,8–11</sup> Furthermore, many applications impose independent requirements<sup>2</sup> on  $T$  and  $R_{sq}$  which cannot be captured by a single FOM value.

In our composite TCEs,  $T$  and  $R_{sq}$  of the TCE are primarily determined by the AgNW layer;<sup>3</sup> thus, we focus on optimizing the spin-coating process of AgNWs using machine-learning (ML) methods to guide the search through processing parameter space. To be useful in most PV and LED applications, we aim to find processing conditions giving TCEs with  $T \geq 75\%$  and  $R_{sq} \leq 15 \Omega/\text{sq}$  simultaneously.<sup>12</sup> Here, the  $T$  value is referenced to air, i.e., transmittance through the TCE layer and PET substrate, not the value referenced to the substrate as often done in the literature.<sup>4,8–10</sup> This total transmittance, which is less than 89% transmittance of bare PET, is what is relevant for PV and LED applications.

As described in detail in the Supporting Information, AgNWs (Figure S1) in ethanol were spin-coated onto PET substrates. After spin coating, the AgNW layer is sintered by photonic curing<sup>13,14</sup> using conditions held constant for this study. Processing involves three variables: AgNW concentration (mg/mL), spin-coating speed (rpm), and dispense volume ( $\mu\text{L}$ ), which form a vector  $X = [\text{concentration, spin speed, volume}]$  in a three-dimensional input parameter space. The measured output objectives for each sample are  $T$ , total transmittance averaged from 400 to 700 nm, and  $R_{sq}$  measured by a four-point probe. We implement an ML framework with multiobjective optimization for this problem, which involves mapping the domain of  $X$  vectors onto a two-objective output. Learning is done in four iterative rounds. Figure 1(a) shows the workflow of the learning process.

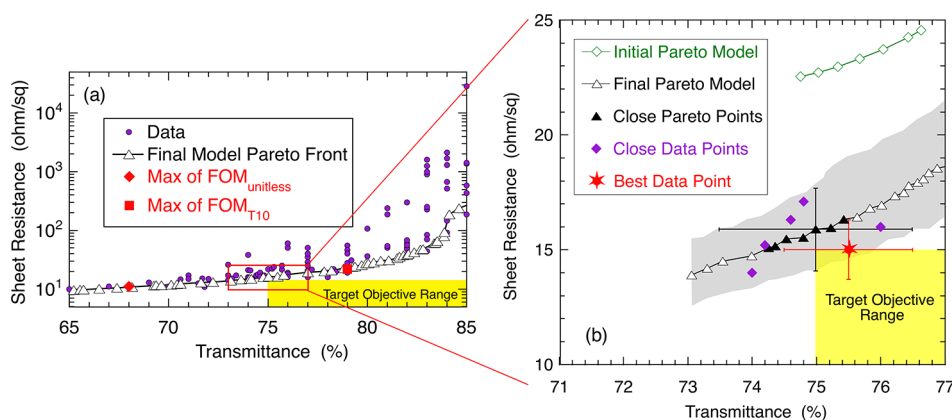
With no prior information, the initial (1st) round synthesizes 36 samples using a set of  $X$  randomly selected by Latin hypercube sampling (LHS) over a three-dimensional domain bounded by arbitrarily chosen (“best guess”) upper and lower limits. Objective data measured on these samples are

used to construct two independent Gaussian process regression<sup>15</sup> (GPR) models, one for  $T$  and one for  $G_{sq}$ . Separate models for  $T$  and  $G_{sq}$  are built because these different physical quantities may have different kernel length scale and amplitude dependencies on  $X$ . We then perform a multiobjective regression analysis using these GPR models to identify subspaces of the input parameter domain having a high probability of improving  $T$  and  $G_{sq}$ . Three subsequent rounds of sample synthesis and measurement are conducted. Each round uses input parameters from promising subspaces provided by the ML analysis, with data updated from prior rounds. In total, 105 samples are synthesized (Table S1 of the Supporting Information). This ML-guided experimental iterative approach enables us to achieve the goal more quickly and with greater confidence than intuitive or trial-and-error approaches.

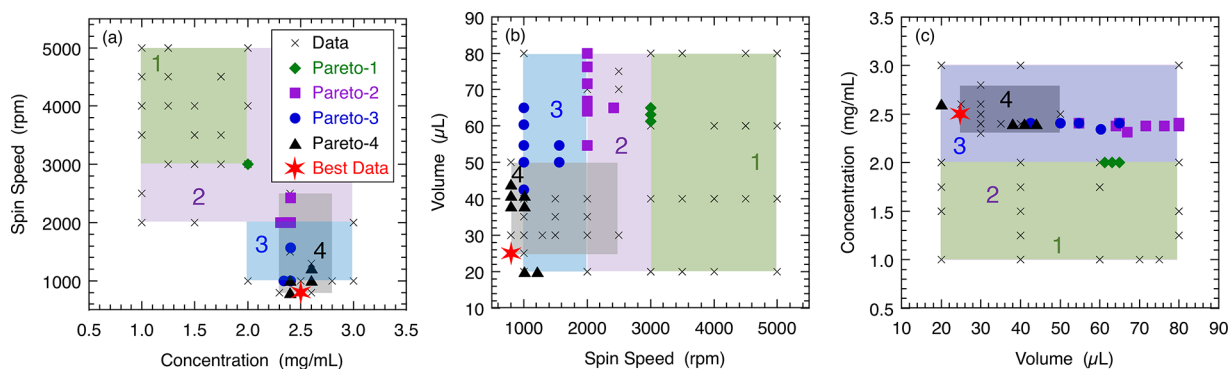
Experimental data are input to a MatLab program using MatLab’s built-in “fitrgp” function to build the GPR models. Details of the options used in fitrgp are given in the Supporting Information. Three-dimensional heat map representations of the GPR posterior mean functions using all 105 data points are shown in Figure S2, and the associated measured vs modeled parity plots computed for  $T$  and  $G_{sq}$  are shown in Figure 1(b) and (c), respectively. Both parity plots exhibit near-unity slope and goodness-of-fit  $r^2$  values, indicating the GPR models are good representations of the underlying data. The modeled global maximum  $T = (85.9 \pm 1.6)\%$  occurs at  $X_T = [1.5 \text{ mg/mL, 3200 rpm, } 20 \mu\text{L}]$ , while the modeled global maximum  $G_{sq} = (0.109 \pm 0.007) \Omega^{-1}/\text{sq}$  (or  $R_{sq} = (9.19 \pm 0.055) \Omega/\text{sq}$ ) occurs at  $X_G = [3.0 \text{ mg/mL, 1200 rpm, } 70 \mu\text{L}]$ . It is clear from these results that maximizing  $T$  requires very different processing conditions than maximizing  $G_{sq}$ . Achieving high  $T$  requires low concentrations and volumes and high spin speeds, while obtaining high  $G_{sq}$  requires high concentrations and volumes and low spin speeds, demonstrating the competing nature of these physical quantities.

Table 1. Predicted Parameters Maximizing Different FOMs Based on GP Models

	AgNW concentration (mg/mL)	Spin speed (rpm)	Dispense volume ( $\mu\text{L}$ )	$T$ (%)	$R_{\text{sq}}$ ( $\Omega/\text{sq}$ )	Max FOM value
$\text{FOM}_{\text{unitless}}$	3.0	800	40	$68 \pm 2$	$11 \pm 1$	$82 \pm 8$
$\text{FOM}_{T_{10}}$ ( $1/\Omega$ )	2.3	1200	28	$79 \pm 2$	$22 \pm 3$	$(4.2 \pm 1.0) \times 10^{-3}$



**Figure 2.** Sheet resistance vs transmission Pareto front. (a) Data from all four experimental rounds (purple dots), the modeled Pareto front (open black triangles), and the modeled points that maximize  $\text{FOM}_{\text{unitless}}$  (red diamond) and  $\text{FOM}_{T_{10}}$  (red square). The yellow shaded region indicates the target range of the objectives. (b) Expanded view of the region indicated in (a) showing the modeled Pareto front after the initial (open green diamonds) and fourth and final (black triangles) experimental rounds. For the final Pareto front, the seven points closest to the target objective range are highlighted as filled black triangles. The gray shaded region indicates the uncertainty about the modeled Pareto front, i.e., the area defined by  $\pm$  one standard deviation of all points on the Pareto front, with one example shown as black error bars. Purple diamonds are the experimental data points closest to the target objective range. The red star indicates the measurement in the target objective range with error bars showing experimental uncertainties in  $T$  and  $R_{\text{sq}}$ .



**Figure 3.**  $X$  inputs of data and modeled Pareto front points closest to target objective range in experimental Rounds 1–4.  $X$  coordinates are projected onto three coordinate planes: (a) spin speed vs concentration, (b) volume vs spin speed, and (c) concentration vs volume. In each plane, the experimental domains of Rounds 1, 2, 3, and 4 are shaded green, purple, blue, and gray, respectively, and labeled with the round number. Domains of different rounds often overlap. The black triangles labeled “Pareto-4” are the  $X$  inputs corresponding to the filled black triangles on the final Pareto front model in Figure 2(b). The  $X$  inputs corresponding to the best experimental result in Figure 2(b) are indicated by a red star.

The GPR models are then combined in a regression analysis in two ways. The more conventional approach uses eq 1 or 2 to predict maximum values of  $\text{FOM}_{\text{unitless}}$ <sup>6</sup> or  $\text{FOM}_{T_{10}}$ <sup>7</sup> and the associated optimal input  $X$ . This approach replaces the two competing objectives with a scalar objective, so that standard Bayesian optimization approaches can be applied. The second approach uses the two models to construct a Pareto front, i.e., the boundary in a modeled  $T$  vs  $R_{\text{sq}}$  plot on which neither objective can be improved without degrading the other, a construction commonly used to analyze trade-offs.<sup>16</sup> We find that simply optimizing FOM cannot achieve the independent requirements on minimum  $T$  and maximum  $R_{\text{sq}}$ , but the Pareto analysis is able to identify the input parameter(s) that achieves the individual objective goals of  $T \geq 75\%$  and  $R_{\text{sq}} \leq 15 \Omega/\text{sq}$ .

Table 1 summarizes the values of  $X$ ,  $T$ , and  $R_{\text{sq}}$  at the modeled maximum of each FOM. Figures S3 and S4 in the Supporting Information show heat maps of projected maximum values and standard deviations of both FOMs. The  $X$  value for maximum  $\text{FOM}_{\text{unitless}}$  occurs at higher concentration and volume and lower spin speed compared to that for maximum  $\text{FOM}_{T_{10}}$ , reflecting the different emphasis of each scalar FOM. From Table 1, if we were to optimize processing conditions based on maximizing FOM, the individual objective goals for  $T$  and  $R_{\text{sq}}$  would not be satisfied. The  $T$  value that maximizes  $\text{FOM}_{\text{unitless}}$  is substantially below 75%, and the  $R_{\text{sq}}$  value that maximizes  $\text{FOM}_{T_{10}}$  significantly exceeds  $15 \Omega/\text{sq}$ .

To determine whether the individual objective criteria can be simultaneously satisfied and, if so, at what input  $X$ , we use

Table 2. Input Parameter Domains as Learning Progresses<sup>a</sup>

	AgNW concentration (mg/mL)	Spin speed (rpm)	Dispense volume ( $\mu\text{L}$ )	# of Data points	Total # of data
Initial LHS (Round 1)	1–2 ( $\Delta = 0.25$ )	3000–5000 ( $\Delta = 500$ )	20–80 ( $\Delta = 20$ )	36	36
Round 2	1–3 ( $\Delta = 0.5$ )	2000–5000 ( $\Delta = 1000$ )	20–80 ( $\Delta = 20$ )	15	51
Round 3	1–3 ( $\Delta = 0.5$ )	1000–2000 ( $\Delta = 1000$ )	20–80 ( $\Delta = 20$ )	16	67
Zoom-in (Round 4)	2.3–2.8 ( $\Delta = 0.1$ )	800–2500 ( $\Delta = 200$ )	25–50 ( $\Delta = 5$ )	38	105

<sup>a</sup> $\Delta$  is the experimental step size.

the GPR models to calculate a two-objective Pareto front.<sup>16</sup> The input  $X$  values associated with those points on the Pareto front closest to the target objective range identify the subspace of processing conditions most likely to strike the desired trade-off between sufficiently high  $T$  and sufficiently low  $R_{\text{sq}}$ .

Figure 2(a) plots  $R_{\text{sq}}$  vs  $T$  data points and a modeled Pareto front after the fourth and final experimental round (105 data points). A definitive Pareto front with all data to its upper left clearly shows the trade-off between increasing  $T$  and decreasing  $R_{\text{sq}}$ . As  $T$  increases above 80%,  $R_{\text{sq}}$  increases drastically; on the other hand,  $R_{\text{sq}}$  never decreases much below 10  $\Omega/\text{sq}$  even at great sacrifice to  $T$ . The target objective range ( $T \geq 75\%$  and  $R_{\text{sq}} \leq 15 \Omega/\text{sq}$ ) is shown as the yellow shaded region. The modeled  $T$ ,  $R_{\text{sq}}$  values that maximize  $\text{FOM}_{\text{unitless}}$  (red diamond) and  $\text{FOM}_{\text{T10}}$  (red square) are plotted; these are well outside the target objective range. Figure 2(b) zooms in on the region where the Pareto front comes closest to the upper left corner of the target range and the experimental results (purple diamonds) that are closest to the target objective range. The difficulty of this materials synthesis problem is clearly evident by the fact that the final Pareto front itself does not overlap the target objective range but is within one standard deviation of the target range. This indicates that achieving both target objective criteria is at the edge of what is possible.

Figure 2(b) also shows the modeled Pareto front after the initial experimental round (open green diamonds). This initial Pareto model is far from the target objective range because the  $X$  inputs for Round 1 were essentially guesses. The final Pareto front is substantially optimized and is much closer to the target objective range. The optimization process conducted over four experimental rounds is graphically depicted in Figure 3, which projects  $X$  vectors onto three coordinate domain planes. The projected  $X$  vectors for the data are marked by  $\times$  symbols. The projected  $X$  vectors corresponding to modeled Pareto points closest to the target range after each experimental round (for example the solid black triangles in Figure 2(b) after the final Round 4) are shown as solid symbols.

The  $X$  values for the closest Round 1 modeled Pareto points (green diamonds in Figure 3) cluster at the highest concentration (2 mg/mL) and lowest spin speed (3000 rpm) in the initial domain, suggesting significant potential improvement by both increasing concentration and reducing spin speed (see Table 2). As stated previously, because the Pareto front after Round 1 is very far from the target range, only the three closest Pareto points are shown in Figure 3. Round 2 adds 15 data points with the maximum concentration increased to 3 mg/mL, and the minimum spin speed decreased to 2000 rpm. From the purple squares in Figure 3(a) and (c), the model indicates after Round 2 the optimal concentration is near 2.5 mg/mL, but the Pareto points closest to the target objective still cluster at the lowest spin speed, suggesting further improvements with even lower spin speed. Round 3 adds 16 data points with a minimum spin speed dropped to

1000 rpm. The blue circles in Figure 3(a) and (c) confirm optimal concentration near 2.5 mg/mL but again mostly cluster at the lowest spin speed used.

The model's suggestion for the best solution volume is less clear. After Rounds 1 and 2, Figure 3(b) and (c) shows the volumes generating Pareto points closest to the target objective are spread over a fairly wide interval of 60–80  $\mu\text{L}$ . After Round 3, the best suggested volume interval is still spread out but appears to shift down to  $\sim 40$ –60  $\mu\text{L}$ . One possibility for the larger spread of volumes is that Pareto points near the target objective range are much less sensitive to volume compared to concentration and spin speed.

Round 4 (final round) of the experiment runs into real-world limitations. We find that making consistent, uniform films requires spin speed  $\geq 800$  rpm and dispense volume  $> 20 \mu\text{L}$ . Respecting these limitations and using the GPR/Pareto model as a guide, we perform final optimization experiments and make 38 samples with  $X$  in the subspace [2.3–2.8 mg/mL, 800–2500 rpm, 25–50  $\mu\text{L}$ ], represented by the gray shaded rectangle in Figure 3. Results closest to the target objective range ( $T$  between 74% and 76% and  $R_{\text{sq}}$  between 14 and 17  $\Omega/\text{sq}$ ) are plotted as purple diamonds in Figure 2(b). One sample (red star in Figure 2(b)) meets both criteria simultaneously, having  $T = 75.5\%$  and  $R_{\text{sq}} = 15.0 \Omega/\text{sq}$ . The  $X$  vector ([2.5 mg/mL, 800 rpm, 25  $\mu\text{L}$ ]) for this “best” data point is marked with a red star in Figure 3. The learning progression through Rounds 1–4 is summarized in Table 2.

In conclusion, we apply an ML-based Pareto front analysis to optimize the spin-coating of AgNWs for flexible TCEs. While scalar FOMs are commonly used in the TCE field, we show optimizing an FOM is inadequate because transmittance and sheet resistance compete with each other, and separate criteria for each must be satisfied. In this case, performing a multiobjective optimization by constructing a Pareto front is necessary. Guided by the ML/Pareto analysis, we successfully identified the input parameter space that satisfies the goal of  $T \geq 75\%$  and  $R_{\text{sq}} \leq 15 \Omega/\text{sq}$ . Further improvement can result from including more input variables, e.g., different AgNWs, coating methods, or photonic curing conditions. More broadly, a ML/Pareto analysis is applicable to other optimization problems when two or more independent criteria must be simultaneously satisfied.

## ■ ASSOCIATED CONTENT

### Supporting Information

3D animations of all experimental data points, and  $T$  and  $G_{\text{sh}}$  models are available in MP4 files. MatLab codes and data are available on GitHub: <https://github.com/UTD-Hsu-Lab/AgNW-Pareto>. The Supporting Information is available free of charge at <https://pubs.acs.org/doi/10.1021/acsnm.3c03599>.

Experimental details, all experimental data, details on GPR and Pareto front calculations, 3D heat map

representation of GPR model, and mean and standard deviation values of  $FOM_{\text{unitless}}$  and  $FOM_{T10}$  (PDF)

Experimental data points (MP4)

3D animation of  $T$  model (MP4)

3D animation of  $G_{\text{sh}}$  models (MP4)

## AUTHOR INFORMATION

### Corresponding Author

Julia W. P. Hsu – Department of Materials Science and Engineering, University of Texas at Dallas, Richardson, Texas 75080, United States; [orcid.org/0000-0002-7821-3001](https://orcid.org/0000-0002-7821-3001); Email: [jwhsu@utdallas.edu](mailto:jwhsu@utdallas.edu)

### Authors

Mark Lee – Department of Physics, University of Texas at Dallas, Richardson, Texas 75080, United States; [orcid.org/0000-0001-6541-8465](https://orcid.org/0000-0001-6541-8465)

Robert T. Piper – Department of Materials Science and Engineering, University of Texas at Dallas, Richardson, Texas 75080, United States; [orcid.org/0000-0002-4032-0602](https://orcid.org/0000-0002-4032-0602)

Bishal Bhandari – Department of Physics, University of Texas at Dallas, Richardson, Texas 75080, United States; [orcid.org/0009-0007-3915-6263](https://orcid.org/0009-0007-3915-6263)

Complete contact information is available at: <https://pubs.acs.org/10.1021/acsnm.3c03599>

### Author Contributions

R.T.P. and J.W.P.H. conceived the idea for the study. R.T.P. designed the experiment. Both R.T.P. and B.B. carried out the experiments. M.L. wrote the MatLab codes. M.L. and J.W.P.H. tested the codes on the experimental data. J.W.P.H. wrote the first draft of the manuscript. All authors discussed the data and edited the manuscript. All authors have given approval to the final version of the manuscript.

### Funding

This work is supported by NSF CMMI-2109554. R.T.P. and B.B. are partially supported by the U.S. Department of Energy's Office of Energy Efficiency and Renewable Energy under the Solar Energy Technologies Office Award Number DE-EE0009518. J.W.P.H. acknowledges the support of the Texas Instruments Distinguished Chair in Nanoelectronics and of the Simons Foundation Pivot Fellowship.

### Notes

The authors declare no competing financial interest.

## ACKNOWLEDGMENTS

We thank Energy Materials Corporation for providing the PET substrates.

## REFERENCES

- (1) Lee, H. B.; Jin, W. Y.; Ovhal, M. M.; Kumar, N.; Kang, J. W. Flexible Transparent Conducting Electrodes Based on Metal Meshes for Organic Optoelectronic Device Applications: A Review. *Journal of Materials Chemistry C* **2019**, *7*, 1087–1110.
- (2) Nguyen, V. H.; Papanastasiou, D. T.; Resende, J.; Bardet, L.; Sannicolo, T.; Jiménez, C.; Muñoz-Rojas, D.; Nguyen, N. D.; Bellet, D. Advances in Flexible Metallic Transparent Electrodes. *Small* **2022**, *18* (19), 2106006.
- (3) Piper, R. T.; Xu, W.; Hsu, J. W. P. Silver Nanowire-Indium Zinc Oxide Composite Flexible Transparent Conducting Electrodes Made by Spin-Coating and Photonic Curing. *MRS Adv.* **2023**, *8* (5), 177–182.

(4) Anand, A.; Islam, M. M.; Meitzner, R.; Schubert, U. S.; Hoppe, H. Introduction of a Novel Figure of Merit for the Assessment of Transparent Conductive Electrodes in Photovoltaics: Exact and Approximate Form. *Adv. Energy Mater.* **2021**, *11* (26), No. 2100875.

(5) Sepulveda-Mora, S. B.; Cloutier, S. G. Figures of Merit for High-Performance Transparent Electrodes Using Dip-Coated Silver Nanowire Networks. *J. Nanomater.* **2012**, *2012*, 1–7.

(6) Dressel, M.; Gruner, G. *Electrodynamics of Solids: Optical Properties of Electrons in Matter*; Cambridge University Press, 2002, 409–416.

(7) Haacke, G. New Figure of Merit for Transparent Conductors. *J. Appl. Phys.* **1976**, *47* (9), 4086–4089.

(8) De, S.; Higgins, T. M.; Lyons, P. E.; Doherty, E. M.; Nirmalraj, P. N.; Blau, W. J.; Boland, J. J.; Coleman, J. N. Silver Nanowire Networks as Flexible, Transparent, Conducting Films: Extremely High DC to Optical Conductivity Ratios. *ACS Nano* **2009**, *3* (7), 1767–1774.

(9) Scheideler, W. J.; Smith, J.; Deckman, I.; Chung, S.; Arias, A. C.; Subramanian, V. A Robust, Gravure-Printed, Silver Nanowire/Metal Oxide Hybrid Electrode for High-Throughput Patterned Transparent Conductors. *J. Mater. Chem. C Mater.* **2016**, *4* (15), 3248–3255.

(10) Van De Groep, J.; Spinelli, P.; Polman, A. Transparent Conducting Silver Nanowire Networks. *Nano Lett.* **2012**, *12* (6), 3138–3144.

(11) DiGregorio, S. J.; Miller, C. E.; Prince, K. J.; Hildreth, O. J.; Wheeler, L. M. All-Atmospheric Fabrication of Ag–Cu Core–Shell Nanowire Transparent Electrodes with Haacke Figure of Merit  $> 600 \times 10^{-3} \Omega^{-1}$ . *Sci. Rep.* **2022**, *12* (1), 20962.

(12) Fan, X. Doping and Design of Flexible Transparent Electrodes for High-Performance Flexible Organic Solar Cells: Recent Advances and Perspectives. *Adv. Funct. Mater.* **2021**, *31* (8), No. 2009399.

(13) Gerlein, L. F.; Benavides-Guerrero, J. A.; Cloutier, S. G. High-Performance Silver Nanowires Transparent Conductive Electrodes Fabricated Using Manufacturing-Ready High-Speed Photonic Sinterization Solutions. *Sci. Rep.* **2021**, *11* (1), 24156.

(14) Jiu, J.; Nogi, M.; Sugahara, T.; Tokuno, T.; Araki, T.; Komoda, N.; Saganuma, K.; Uchida, H.; Shinozaki, K. Strongly Adhesive and Flexible Transparent Silver Nanowire Conductive Films Fabricated with a High-Intensity Pulsed Light Technique. *J. Mater. Chem.* **2012**, *22* (44), 23561.

(15) Rasmussen, C. E. Gaussian Processes in Machine Learning. In *Advanced Lectures on Machine Learning*; Bousquet, O., von Luxburg, U., Ratsch, G., Eds.; Springer-Verlag, 2004; pp 63–71.

(16) Ngatchou, P.; Zarei, A.; El-Sharkawi, A. Pareto Multi Objective Optimization. In *Proceedings of the 13th International Conference on Intelligent Systems Application to Power Systems*; IEEE, 2005; pp 84–91.